Role of the Secondary Phase η During High-Temperature Compression of ATI 718Plus®

CHRISTIANE KIENL, PARANJAYEE MANDAL, HIMANSHU LALVANI, and CATHERINE M.F. RAE

High-temperature compression tests were performed on a Ni-base superalloy with a multi-phase microstructure. Particular attention was given on the influence of the η phase on recrystallization of ATI 718Plus®. The compression tests were performed at two temperatures over a variety of strains and strain rates. Meta-dynamic recrystallization was studied by exposing the samples to a set dwell time at the test temperature after deformation. Electron backscatter diffraction (EBSD) was used to investigate the microstructures after the tests. Secondary electron imaging (SEI) and scanning transmission electron microscopy (STEM) were utilized in order to investigate the deformation behavior of η and obtaining a detailed understanding of the recrystallization mechanism. The secondary η phase was found to increase the recrystallized fraction compared to η free tests. However, clusters of thin lamellar η inhibited recrystallization. The flow curve softening was distinctly stronger in the microstructure containing precipitates. It could be shown by SE images that this was due to the breakage and realignment of η. In addition, η was also found to accommodate the stresses by a remarkable deformation without breaking up. This was considered to be due to the composite nature of the precipitate as well as the ongoing recrystallization in the surrounding matrix.

https://doi.org/10.1007/s11661-020-05837-7

I. INTRODUCTION

DYNAMIC recrystallization (DRX) is a restorative mechanism of the microstructure which occurs during the forging of an alloy. For critical components such as turbine disks in jet engines, a homogeneous microstructure after the forging is key to prevent failure. Hence, the effect of large pre-existing precipitates on the kinetics of DRX is of great importance.

Ni-base superalloys are the material of choice for turbine disks in the high pressure section of an aero engine. One of which is ATI 718Plus® (hereafter 718Plus), a multi-phase strengthening polycrystalline Ni-base superalloy. Its main strengthening phase is the cubic γ' (Ni_3[Al,Nb,Ti]) which is finely dispersed in the γ matrix. The second precipitate found in 718Plus is the hexagonal η phase (Ni_6[Al,Ti]Nb) which is interlayered with narrow orthorhombic δ (Ni_3Nb).[1,2] The η morphology depends on the thermo-mechanical history of the material and can range from small and blocky to a thin lamellar structure.[3] Such particles could influence the recrystallization characteristics of 718Plus.

718Plus was designed based on Inconel 718 (hereafter IN718) which forms δ phase.[4] Due to its importance in turbine applications, processing of IN718 has attracted a considerable amount of attention. δ phase was found to enhance the rate of dynamic recrystallization.[5,6] The proposed mechanisms for this observation ranged from boundary bulging as observed during DRX, particle stimulated nucleation (PSN) to a microstructural refinement due to grain splitting and rotation.[7,8] PSN is the recrystallization around particles because of the increased dislocation density during deformation in these zones compared to particle-free areas. PSN is commonly found during static recrystallization and includes the formation of subgrains and subsequent growth around particles larger than ~ 1 μm.[9] Lalvani *et al.*[10] observed a grain refinement during high-temperature compression testing of a γ–δ microstructure. They related it to the partial disintegration and rotation of grain segments. DRX was found in particle-free areas suggesting that the precipitates hinder the progress of DRX. In contrast, Wang *et al.*[11] reported an increase of recrystallization if δ is present. The effect of secondary precipitates on the kinetics of DRX is a controversial topic where retardation as well as enhancement are attributed to them.[12]

CHRISTIANE KIENL and CATHERINE M. F. RAE are with the Department of Material Science and Metallurgy, University of Cambridge, 27 Charles Babbage Road, Cambridge CB3 0FS, UK. Contact e-mail: ck492@cantab.ac.uk PARANJAYEE MANDAL and HIMANSHU LALVANI are with the Advanced Forming and Research Centre, University of Strathclyde, 85 Inchinnan Drive, Renfrew PA4 9LJ, UK.

Manuscript submitted February 2, 2020.
Article published online May 30, 2020

The flow curves of δ-containing microstructures were generally found to exhibit a strong flow softening after the peak stress.[13,14] This effect was attributed to the alignment and rearrangement of δ with the material flow. While δ was found to break up and spheroidize in IN718[15–17] other δ containing alloys only showed the alignment of the precipitates.[14,18]

The effect of η on DRX during high-temperature deformation of 718Plus has not yet been analyzed. The present study will address the changes in flow behavior and recrystallization kinetics by means of electron backscatter diffraction (EBSD) and secondary and backscattered electron imaging (SEI, BSE) in a scanning electron microscope (SEM). Transmission electron microscopy (TEM) was utilized to investigate local effects of recrystallization around η particles.

II. MATERIALS AND METHODS

The material for this analysis was extracted from a 718Plus billet (chemical composition in Table I) which was manufactured by ATI Specialty Metals and supplied by Rolls–Royce Deutschland. The production of the ingot followed the standard procedure of a triple melt (vacuum induction melt/VIM, electro slag remelt/ESR, vacuum arc remelt/VAR) and was then cogged into a billet with 220 mm diameter.

High-temperature compression tests were performed at the Advanced Forming Research Centre at the University of Strathclyde. The compression samples were 10 × 15 mm cylinders with flat surfaces on both ends. As the as-received microstructure was η free, a heat treatment was given according to a time-temperature-transformation (TTT) diagram for 718Plus.[20] A precipitate volume fraction of 4 vol pct was chosen and therefore the heat treatment was at 975 °C for 10 hours followed by a water quench. A servo-hydraulic testing machine Zwick Z250 was utilized to perform the tests. The testing procedure required the furnace to be preheated to 650 °C at which point the samples were placed between the dies. With heating rate of 12 °C min^{-1} the temperature was raised to the respective testing temperature, which was maintained within ± 2 deg. Before the compression, the samples were kept at the testing temperature for 15 min. The compressed specimens were water quenched within 5 seconds after the test. Some samples were kept in the furnace after compression for 120 seconds in order to promote the meta-dynamic recrystallization. The full test matrix is shown in Table II.

For microstructural characterization the samples were sectioned half parallel to the loading axis. While one half was mounted in conducting Bakelite for secondary electron microscopy (SEM) analysis, the other half was cut into thin plates from which spark-eroded transmission electron microscopy (TEM) disks were produced. The SEM samples were further ground, polished, and given a finish with oxide polishing suspension (OPS) to reach the good surface quality necessary to acquire an electron backscatter pattern (EBSP). After electron backscatter diffraction (EBSD) analysis some samples received a γ etch to excavate η for topological studies in the SEM. These specimens were electro-chemically etched with 10 pct orthophosphoric acid in distilled water at 10 V. The TEM disks were electropolished to obtain an electron transparent region with a solution of 6 vol pct perchloric acid in methanol at − 5 °C.

The SEM used in this study was a Zeiss Gemini 300. The secondary electron (SE) analysis was performed at 5 keV acceleration voltage and backscatter electron (BSE) and EBSD at 25 keV. For EBSD, the samples were tilt to 70 deg and the step size of the scans was 15 μm. The transmission Kikuchi diffraction (TKD) analysis was done with the same acceleration voltage but the step size was decreased to 0.15 μm. The EBSD data was analyzed with Oxford Instruments' HKL Channel 5 software and the MTEX toolbox for MATLAB. Automatic detection of η on the BSE images was unsuccessful due to a strong deformation contrast. Hence, the precipitates were manually redrawn and scanned to further process them with ImageJ.[21]

Bright-field (BF) TEM was performed on a JEOL 200CX operating at 200 keV. Electron-dispersive X-ray spectroscopy (EDX) of the η particles was done in scanning transmission electron microscopy (STEM) mode on a FEI Osiris at the same acceleration voltage.

III. RESULTS

The kinetics of recrystallization depends on the initial microstructure[9]. Therefore, the η microstructure before the compression test was characterized in terms of grain size and η content. Figure 1(a) shows an inverse pole figure map (IPF) in the out-of-plane direction from an EBSD scan of a sample after the η-heat treatment. The grain boundaries with a misorientation angle 15 deg are drawn in black and the first-order twin boundaries following the Brandon criterion are in red.[22] The grain size excluding twin boundaries after the 10 hour η heat treatment was 36 ± 28 μm. Figure 1(b) presents a BSE image of the initial microstructure. The morphology of the η particles is thin lamellae which were frequently found to form clusters. These clusters appear to be orientated in the same direction within a grain and the clusters orientation differs from grain to grain.

In a previous study, the η-free γ–γ' microstructure of 718Plus was analyzed after testing with the same conditions used in the current work.[23] Hence, these results will be compared with the η-containing microstructure where applicable. The samples for both microstructures were extracted from the exact same billet material in the diaphragm of the disk. However, the grain size at the start of the compression test was slightly larger at 43 ± 27 μm for the η-free microstructure due to the lack of grain boundary pinning η precipitates. This measurement was taken on a sample which had received an equivalent heat treatment to the test cycle. The test cycle included a heat-up and dwell of the specimens which summed up to ~ 45 minutes at elevated temperature. Due to the much longer η-heat

Table I. Chemical Composition of ATI 718Plus® in Wt Pct[19]

	Ni	Cr	Mo	W	Co	Fe	Nb	Ti	Al	C	P	B
718Plus	bal.	18.0	2.75	1.0	9.0	10.0	5.45	0.7	1.45	0.020	0.014	0.004

Table II. Test Matrix for High-Temperature Compression Tests on η Containing Microstructures

Strain (−)		0.4		0.8			1.2	
Strain rate (s^{-1})		1	0.01	1	0.01	0.1	1	
Temperature (°C)	950	x		x/120	x/120	x	x/120	
	975		x/120	x	x/120		x/120	

Sample pairs 'x/120' refer to specimens which were kept in the furnace where the '120'-sample has been annealed.

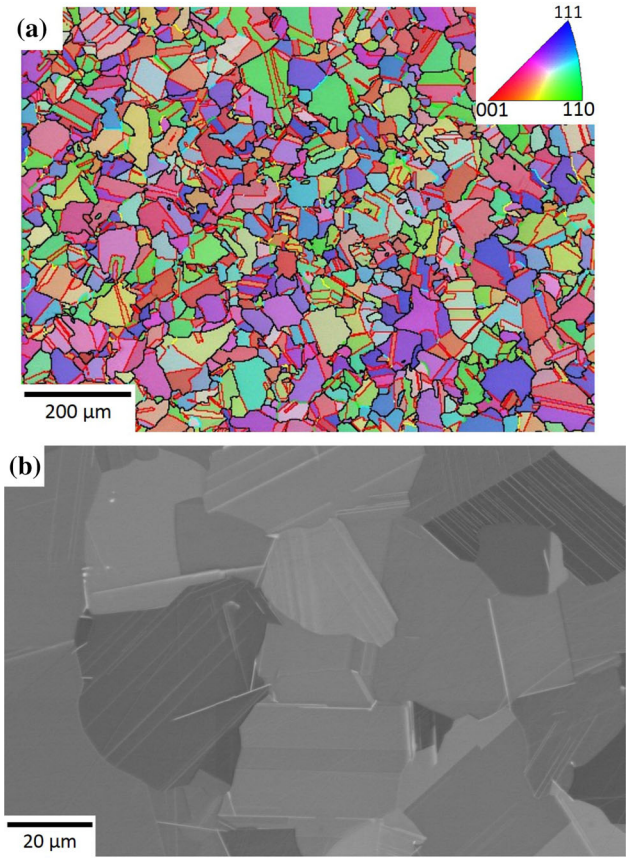

Fig. 1—Pre-deformation η microstructure. (*a*) IPF map in out-of plane direction with highlighted grain boundaries (*b*) BSE image with thin elongated needle-like η appear bright (Color figure online).

treatment the microstructural changes during the testing cycle were assumed to be negligible.

The microstructure analyzed after the tests contained only the γ matrix and η precipitates. The γ' particles completely dissolved during the test as their solvus temperature is 967 °C which was within the testing regime.[20] They neither appeared in the etched SEM samples nor could they be detected as superlattice diffraction spots in the TEM.

The results of the high-temperature compression tests will be presented in three parts. Firstly, the stress–strain curves will show the flow behavior of the γ–η microstructure. Secondly, the recrystallization kinetics of 718Plus will be characterized quantitatively by means of EBSD. Finally, the deformation characteristics of η during the compression test will be presented.

A. *Flow Behavior*

Flow curves were calculated from the load-stroke data provided. The stroke reading was corrected for offsets at the initial loading of the sample, machine compliance and the thermal expansion of the specimen. From the adjusted data the stress–strain curves were calculated and corrected for friction between sample and compression dies and adiabatic heating. Figure 2 shows the flow curves for the samples compressed to the maximum strain of 1.2 for the temperatures 950 °C and 975 °C at the three strain rates tested. The dotted lines are the stress–strain curves of the respective tests with the η-free microstructure.

All curves start with the typical linear-elastic region which terminates at the yield point. Following the yield point, the curves for the lower strain rates show a yield point drop before they rise again. While the tests at a strain rate of 0.01 s^{-1} had yield point drops for both the η and η-free conditions, the yield point drop is absent for the η microstructure tested at 950 °C at a strain rate of 0.1 s^{-1}. During the subsequent work-hardening stage the dislocation density increases and thus hinders further movement. In parallel to the work hardening the microstructure recovers dynamically and recrystallization starts to evolve. The peak stress marks the point at which the rate of softening equals the effect of work hardening.[9] As for the yield point, the peak stress is similar for the η and η-free microstructures. After the peak stress the flow curves of all tests drop due to the increase in dynamic recrystallization. However, the η-containing samples exhibited a slightly stronger flow curve softening and this is dominant at the higher temperature (975°C) and strain rate (1 s^{-1}).

Table III presents the measured mechanical properties from both microstructures. The yield point increases for η-free and η-containing samples with higher strain

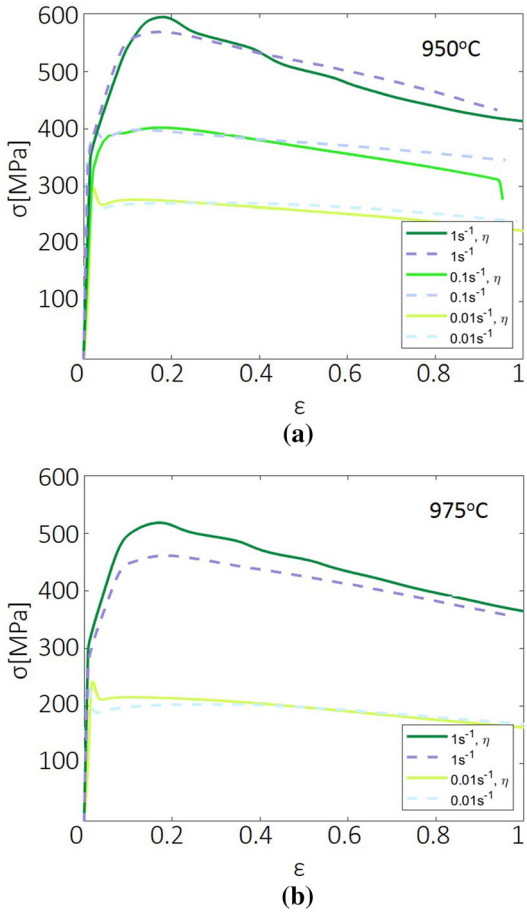

Fig. 2—Stress–strain curves of the η and η-free microstructures at strain rates of 0.01, 0.1, and 1 s^{-1} and temperatures of (*a*) 950 °C and (*b*) 975 °C (Color figure online).

rates and decreases with temperature. Comparing the values of the two microstructures the η samples tend to have higher yield stresses. An exception is the test at 950 °C and 0.1 s^{-1} strain rate where σ_Y of the η-free specimen is 6 MPa higher than the η equivalent. The ultimate strength σ_P in the η-containing microstructure in general exceeds that of the η-free samples.

B. *Quantitative Microstructural Analysis*

In this section, the recrystallization of the two-phase γ–η microstructure will be analyzed. Figures 3(a) and (b) presents the inverse pole figure (IPF) maps perpendicular to the loading axis from EBSD scans for the samples compressed at 950 °C to 1.2 with a strain rate of 0.01 and 1 s^{-1}. Below the IPF maps are the corresponding BSE images of the area with the secondary precipitates redrawn in red. The η precipitates were too thin to be successfully identified by EBSD; thus, the Z(atomic number)-contrast from BSE images were used to distinguish η. From the IPF maps, the recrystallized fraction was calculated using the grain orientation spread (GOS)

$$GOS = \sqrt{\frac{1}{N-1}\sum_{i=1}^{N}(\overline{\Theta_g} - \Theta_{gi})}, \quad [1]$$

where $\overline{\Theta_g}$ is the mean orientation of grain g, Θ_{gi} defines the orientation of a pixel i in grain g and N is the total number of pixels in the grain. A GOS value of 1.2 deg was chosen to determine recrystallized areas from unrecrystallized grains.[24] Table IV presents the recrystallized fraction X_{RX} after dynamic (DRX) and meta-dynamic recrystallization (MDRX) in the top half. The lower half of the table lists the average grain diameters D_{RX} of the recrystallized areas at their respective conditions. Double entries consist of the DRX value followed by a backslash and the MDRX value at these conditions. The recrystallized fraction increases with temperature and strain. Raising the strain rate also enlarges the recrystallized area. However, the specimen compressed with the intermediate strain rate of 0.1 s^{-1} at 950 °C to 1.2 is an exception to this trend.

The evolution of the average recrystallized grain size follows the observed patterns for DRX. The grain sizes grow larger with the testing parameters while the sample at intermediate strain rate shows the same behavior for the recrystallized fraction. All of these results are in-line with the previously reported trends in the single-phase microstructure.[23] However, in absolute numbers the η specimens have a slightly larger area recrystallized than η-free. It should be remembered at this point that the initial grain sizes of the two microstructures were slightly different. Figure 4 shows a comparison of the recrystallized fractions with strain rate of the two microstructures. From this graph, the recrystallization kinetics at the lower strain rates are significantly different from those at high strain rates.

While it was hypothesized that the heterogeneous distribution of the η precipitates might suggest a broad distribution in recrystallized grain size, this was observed to not be the case. Figure 5(a) presents the spread of grain size for the η specimens tested at 950 °C to a strain of 0.8 with strain rates of 0.01 and 1 s^{-1}. The corresponding η-free samples are given in b. In both microstructures the higher strain rate results in a broader grain size distribution compared to the slower. In addition, a clear difference can be seen for the two microstructures. The η containing samples developed a narrower grain size spread than the single-phase specimens at both strain rates.

MDRX is the growth of recrystallized grains at the expense of deformed grains after deformation has ceased. Second-phase particles can influence the growth as well as the dislocation structure available for MDRX. The MDRX fraction is listed in Table IV. In general, recrystallization by MDRX increases with strain, strain rate, and temperature. To analyze the grain size heterogeneity after the 120 seconds dwell at high temperature the size distribution is given in Figure 6. The diagrams present the evolution of grain size with post-deformation dwell time for specimens deformed at 975 °C to a strain of 1.2 with 1 s^{-1}. The η-containing microstructures in green only show small changes in the grain size spread

Table III. Yield Stress σ_Y, Upper and Lower Yield Point ($\sigma_{Y,U}$, $\sigma_{Y,L}$) and Peak Stress σ_P for η-Free and η-Containing Samples Tested to Maximum Strain

Strain (−)	T (°C)	$\dot{\epsilon}$(s^{-1})	σ_Y	$\sigma_{Y,U}$	$\sigma_{Y,L}$	σ_P	$\sigma_{Y,\eta}$	$\sigma_{Y,U,\eta}$	$\sigma_{Y,L,\eta}$	$\sigma_{P,\eta}$	$\lvert\Delta_{\sigma_Y}\rvert$
1.2	950	0.01	268	281	259	271	285	297	268	277	17
		0.1	326	390	384	398	320			402	6
		1	347			568	357			594	10
	975	0.01	212	241	190	203	225	240	211	216	13
		1	294			461	328			518	34

Δ_{σ_Y} is the absolute difference between the yield points of the two microstructures. The stress values are in MPa.

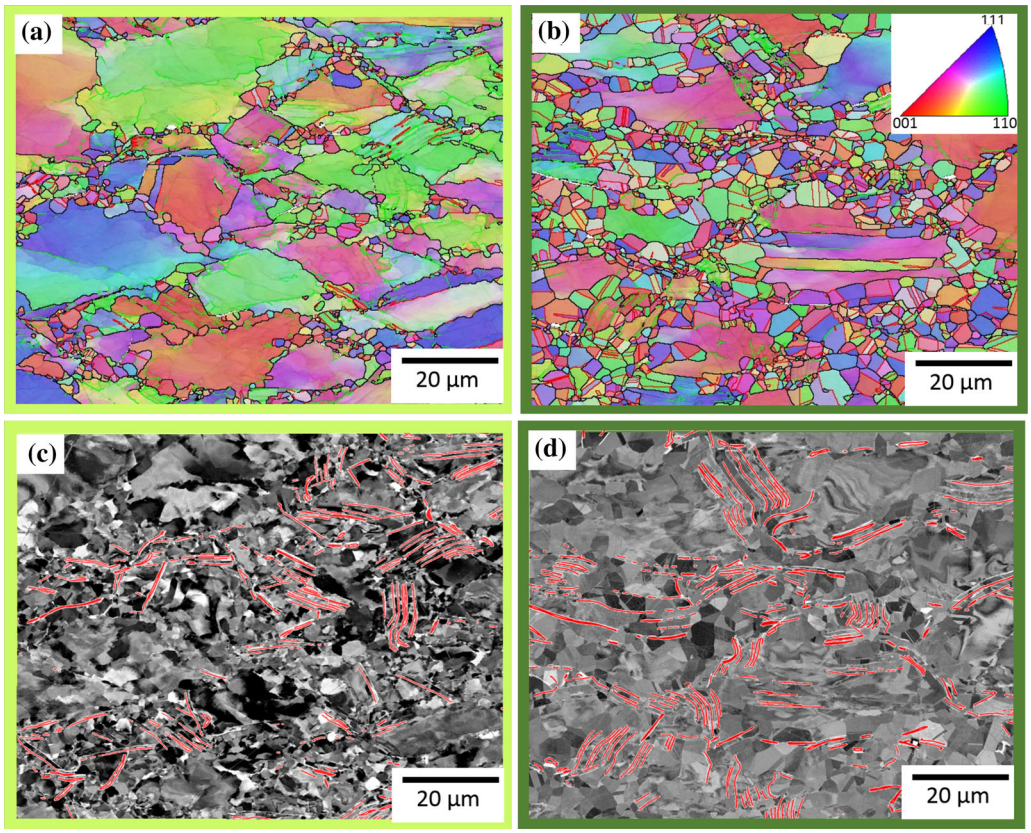

Fig. 3—Microstructures of the compressed samples at 950 °C to a strain of 1.2 and a strain rate of 0.01 s^{-1} (*a* and *c*) and 1 s^{-1} (*b* and *d*). (a) and (b) represent IPF maps and (c) and (d) the corresponding BSE images with η highlighted in red (Color figure online).

Table IV. Recrystallized Fraction and Grain Size of All Tested Samples

Strain [-]			0.4	0.8		1.2		
Strain rate [s^{-1}]			1	0.01	1	0.01	0.1	1
Temperature [°C]	950	$X_{RX,\eta}$ [%]	8		37/66	26/49	25	58/78
	975			20/52.6	70	42/77		76/98
	950	X_{RX} [%]			13/43	19	22	43/77
	975			25/81	43/95	35/90	28	50/95
	950	$D_{RX,\eta}$ [µm]	1.3		1.4/1.8	1/1.1	0.9	2/1.5
	975			1.2/1.7	1.9	1.2/2.2		2.3/2.2

Single entries are DRX, double entries contain of the DRX and MDRX value separated by '/'.

during MDRX. Both microstructures have a descending frequency of grain sizes with the tallest peak at the smallest grains. The MDRX microstructure developed a few grains larger than 7 µm. The η-free samples are given in blue and purple and the differences in grain size variance are significant. The specimens without dwell

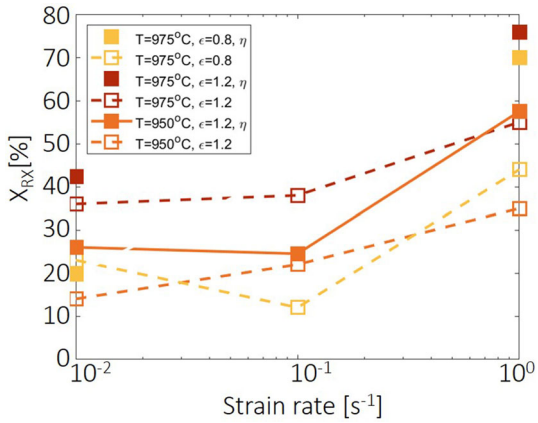

Fig. 4—Evolution of the recrystallized fraction with strain rate for η and η-free tests at different temperatures and strains (Color figure online).

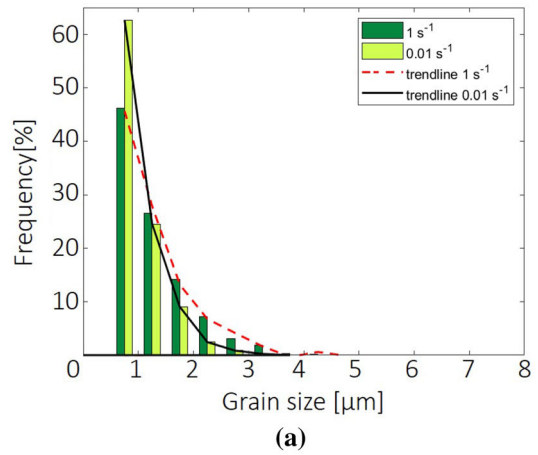

(a)

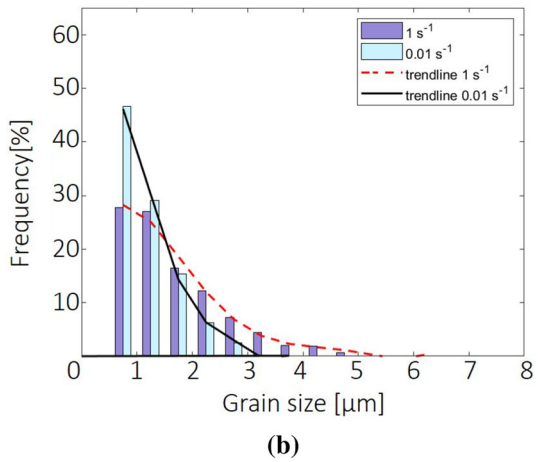

(b)

Fig. 5—Grain size distribution of samples deformed at 950 °C to a strain of 0.8 and strain rates of 0.01 and 1 s^{-1} with the microstructures of (*a*) η and (*b*) η-free (Color figure online).

have a similar distribution to the η-containing microstructure with a plateau at the smallest grain sizes. However, the grain size distribution after 120 s is distinct from η-containing specimens. Even though most

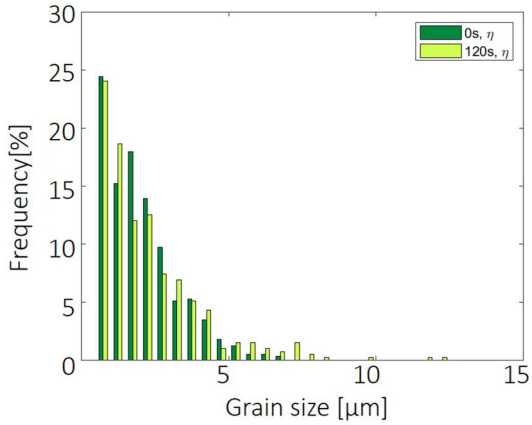

(a)

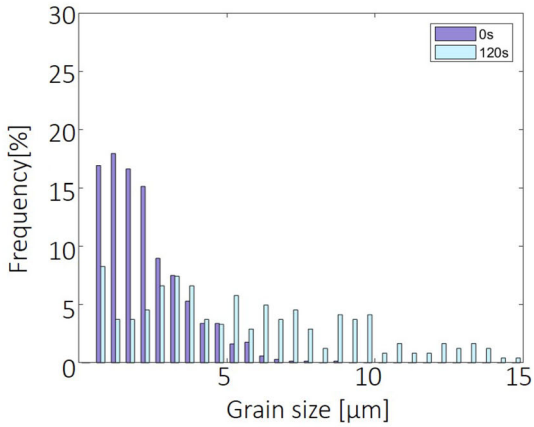

(b)

Fig. 6—Grain size distribution of DRX and MDRX-samples deformed at 975 °C to a strain of 1.2 and strain rates of 1 s^{-1} with the microstructures of (*a*) η and (*b*) η-free (Color figure online).

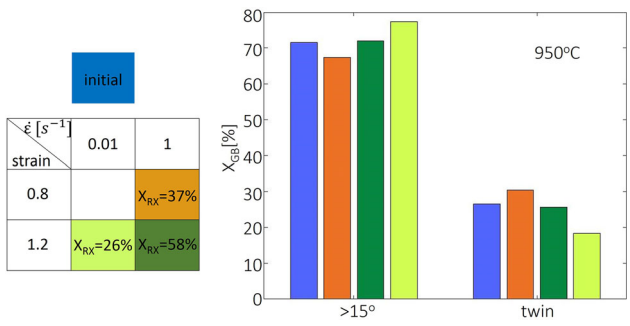

Fig. 7—Evolution of grain boundary misorientation for η samples tested at 950 °C at various strains and strain rates. The grain boundary misorientation was clustered in high angle grain boundaries (>15 deg) and twins (60 ± 8.66 deg ⟨111⟩) (Color figure online).

grains are still smaller than 2.5 μm their proportion, divided between DRX and MDRX has diminished by two-thirds. Several other peaks can be detected with a clear shift to higher grain sizes. The scatter is broader and persists up to the cutoff size of 15 μm. About 3 pct of grains were larger than the cutoff size.

The evolution of the grain boundary misorientation angles for η specimens tested at 950 °C is illustrated in Figure 7. The misorientation angle α was divided into high angle boundaries (HAGB, $\alpha > 15$ deg) and twins ($\alpha = 60 \pm 8.66$ deg $\langle 111 \rangle$.[22]) Higher-order twin boundaries were not considered as they accounted for less than ~ 1 pct of all twins. While deformation twins are too small to be detected by EBSD only annealing twins contribute to the measurement. The fraction of grain boundaries was measured by counting one frequency point per boundary, not per unit length. The blue bar shows the boundary fractions for the initial η microstructure before testing. The green and orange bars are the results for high strain rates and strains of 1.2 and 0.8, respectively, and the light green column refers to the sample tested at a strain rate of 0.01 s^{-1} to 1.2. The legend on the left side of the figure contains the respective recrystallized fractions. Overall it can be seen that the highest recrystallized fraction (dark green) has an almost identical GB distribution to the initial condition (blue). Comparing the influence of strain, the higher strain (green) leads to more HAGBs than a lower strain (orange). The opposite is the case for the development of twin boundaries. Turning to the effect of strain rate, more HAGBs are found at slow strain rates, comparing 0.01 s^{-1} (light green) with 1 s^{-1} (green). Conversely, fewer twin boundaries are present at slower strain rates.

C. *Deformation of η*

The η precipitates in the current study are presented as long, thin precipitates in the 2D section. The following section presents the response of η to the strain induced by the compression tests.

Figure 8 shows the orientation of η with the progression of strain. The initial microstructure in blue shows a homogeneous distribution of η throughout the whole polar histogram. A fraction of about 0.1 η precipitates is aligned horizontally while a fraction 0.05 of the total amount of η is in a vertical position. A similar observation can be made for the specimen compressed to a strain of 0.3 in yellow. Increasing the strain leads to a strong alignment of η with the flow, as shown for the strains of 0.8 in orange and 1.2 in green.

After the general overview of the rearrangement of η, the specific deformation characteristics of η were addressed by analyzing etched samples. Figure 9(a) presents the various ways η adjusted to the strain. At the grain boundaries marked by black arrows, the precipitates are broken up and scattered along the boundaries. In contrast, larger particles on the left have deformed by bending (red arrow). The green arrow highlights dense clusters of η which could prevent the areas in between from recrystallizing. Figure 9(b) shows the breakage of lamellar precipitates known as spheroidization. Another interesting response of η to the strain was a severe bending of the particle as seen in Figure 9(c). While some parts of a horseshoe were formed by smaller parts which have broken up but realigned, the left part in the close-up of Figure 9(c) is found to be just a single folded precipitate. No evidence of cracks or voids associated with the η precipitates was seen.

IV. DISCUSSION

The secondary η precipitates in 718Plus were found to influence the behavior of the alloy during high-temperature compression tests in several ways. The stress–strain curves of the precipitate-containing microstructure experienced a stronger flow softening compared to the single-phase tests. Both microstructures caused a yield point drop more noticeable in case of the η-containing microstructure. The recrystallized fraction during both DRX and MDRX were higher in the two-phase microstructure. Deforming η led to an realignment of

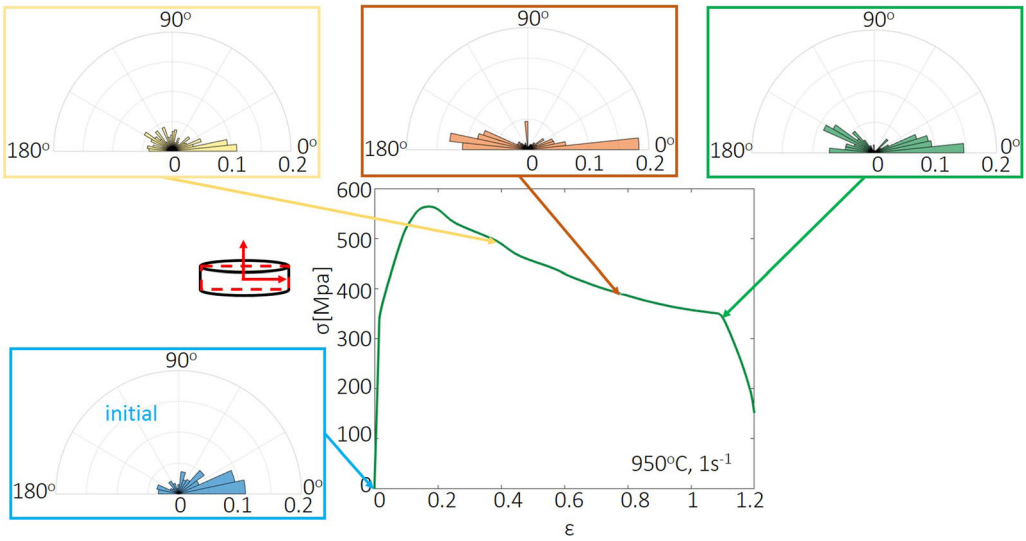

Fig. 8—Alignment of η particles with strain at 950 °C and 1 s^{-1} strain rate. The pole plot shows the relative fraction of η precipitates with respect to their angle (Color figure online).

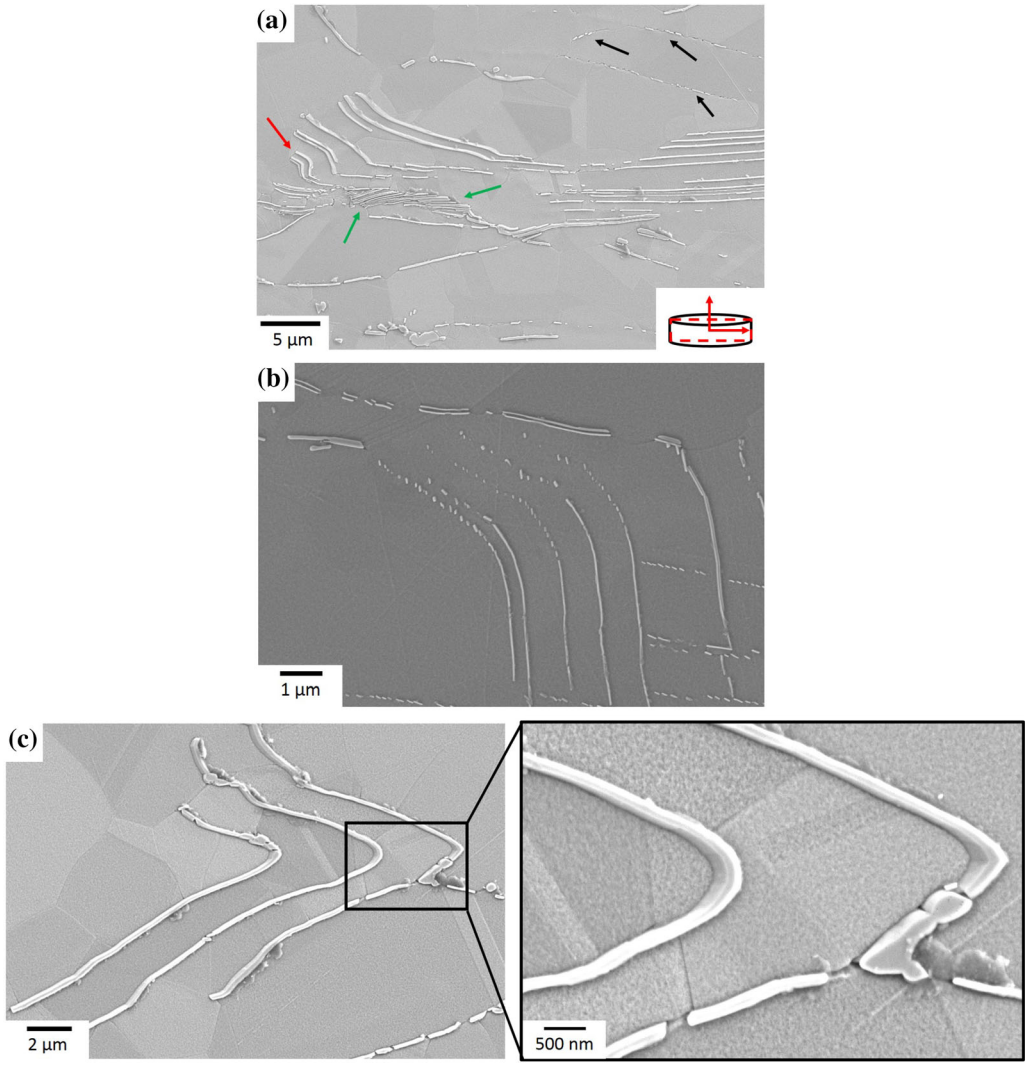

Fig. 9—SEI from γ etched specimens to reveal η. Samples were tested at 975 °C, ϵ 1.2 and dwell time 120 s with a strain rate of 1 s^{-1} (*a* and *c*) and 0.01 s^{-1} (*b*).

the particles together with fragmentation and severe bending of the precipitates.

A. *Flow Characteristics*

Peak and yield stress of both microstructures were similar with the variations being within deviation limits of mechanical testing. The mechanical properties were higher for the η samples in most cases. However, differences in flow curve softening were clearly visible. High-temperature compression tests on δ-containing Ni-base superalloys displayed similar behavior.[7,13] Flow softening can be caused by the progression of dynamic recrystallization. The fraction of DRX at the lowest measured strain of 0.4 amounted to only 8 pct. Hence, the only other cause must be related to the η particles.

The η containing specimens produce a slightly higher yield stress than their single-phase counterparts (Table III). From the characterization of the initial microstructure, the initial grain size between η-free and η specimens differed by ~ 4 μm. Following the well-known relationship by Hall-Petch the microstructure with the smaller grain size (η) results in higher yield stresses. In the Hall-Petch relation the grain size strengthening term is defined as $\frac{k}{\sqrt{d}}$ where k is a material specific constant and d the grain size. For the tested samples the grain size for the η-free microstructure was measured to be 43 μm and in η-containing samples 36 μm. Assuming k to be 1 MPa $m^{1/2}$,[25] the strengthening term for the smaller grain size adds up to 167 MPa. For the larger grain size of 43 μm strengthening by grain boundaries is calculated to reduce by 15 to 152 MPa. The difference in yield stress was on average around this value; hence, the initial grain size seems to be a sufficient reason for this effect. Therefore, the strengthening effect of the η precipitates has appears to have a smaller influence possibly due to the low volume fraction of η. The primary role of η particles is to pin the grain boundaries rather than hinder dislocation movement.

Another phenomenon observed in the flow curves was a yield point drop for samples compressed at lower strain rates and in η-containing sample at the intermediate rate. The relative yield point drop RYD was calculated using the upper and lower yield point $\sigma_{Y,U}$ and $\sigma_{Y,L}$ and is plotted in Figure 10:

$$RYD = \left(1 - \frac{\sigma_{Y,L}}{\sigma_{Y,U}}\right). \quad [2]$$

From Figure 10 it can be seen that for a given temperature, the yield point drop becomes stronger with slower strain rates. These results fit broadly with those of Momeni *et al.*,[26] also plotting the RYD as a function of temperature and strain rate. Both studies show that the maximum yield point drop moves to higher temperatures as the strain rate becomes faster, indicating a thermally activated process.

Such a yield point drop has been reported frequently in Ni-base superalloys such as 718Plus.[26–28] They are often associated with dynamic strain aging, DSA, which is variously associated with dislocation pinning by solutes, γ' precipitates forming on the dislocations, or short-range ordering.[27,29,30] A yield point drop is then attributed to a sudden increase in mobile dislocation density, either by the unpinning of dislocations or by the formation of a dislocation source. We do not think these effects are occurring here as the temperature range over which DSA effects are seen in superalloys peaks at around 700°C and these forging temperatures are 950°C and above. These temperatures are way in excess of the γ' solvus and the short-range ordering temperatures. Furthermore, softening is not due to adiabatic heating as the curves have been corrected for this effect and it is not significant at such low strains. Recrystallization can also be ruled out as, even at 0.4 strain, the fraction recrystallized is a maximum of only 8 pct for the fastest strain rate (Table IV), whereas the yield drop occurs at strains of around 1 pct where DRX is minimal.

A further possibility to explain the yield drop is the formation of twins which have been proposed as a cause of serrated yield in TWIP steels.[31] In a previous paper we have measured the stacking fault energy in 718Plus as 15 mJm^{-2}, an unusually low value for a superalloy.

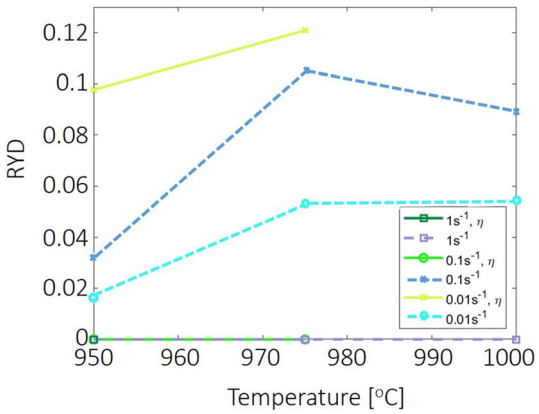

Fig. 10—Relative yield point drop for η and η-free specimens with respect to temperature.

We noted that twinning is a prominent deformation mechanism at these temperatures and strain rates in the η-free microstructure.[32] The extent of twinning in the super-solvus regime was not strongly dependent on temperature and showed a weak increase with strain rate. Although the deformation mechanisms were not examined at or around the yield point, observations of specimens with a strain of 1 show ample evidence of closely spaced micro-twins together with a high dislocation density in the matrix in between. Examination of newly recrystallized grains showed numerous examples of the formation of micro-twins in the early stages of deformation formed from the dissociation of lattice dislocations.[32]

Examination of the η-containing material deformed at 950 °C and the lowest strain rate shows very extensive twinned areas stretching across a single grain, Figure 11. This micrograph shows many parallel twins (marked DT) diagonally across a single grain, the twins often being in excess of 100 nm thick. Such features were common in the microstructure. As the strain in this sample was 1.2 deformation by dislocation movement is also very extensive and recovery of that dislocation structure into distinct cells is also clearly seen. We suggest that the yield drop could be due to the rapid multiplication of twins in the early stages of deformation immediately following yield. Their propagation requires less stress than the nucleation of the twins, resulting in a sudden drop in stress. Twinning can only provide a fraction of the strain and at low strain rates and those twins nucleated could be sufficient to do this, but at the higher strain rates additional simultaneous deformation from lattice dislocations would be necessary. Thus at higher strain rates significant dislocation movement would also be necessary to achieve the strain, requiring the maintenance of an increasing stress to generate this dislocation density. The combination of twinning and extensive dislocation activity in the matrix would give rise to the very high work-hardening rates observed at the higher strain rate and also the lack of a

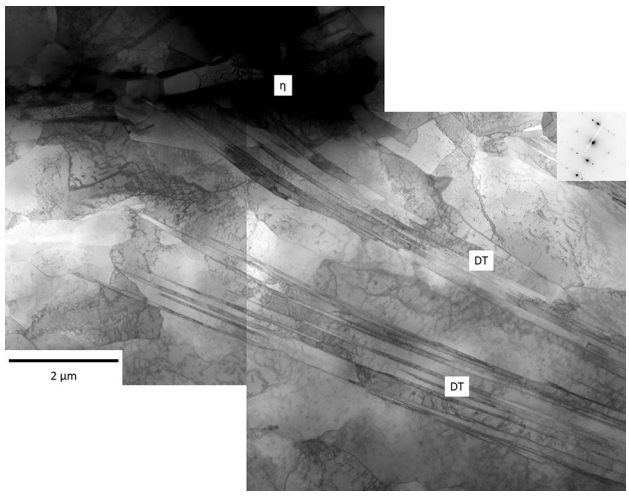

Fig. 11—Highly deformed grain including areas with deformation twins (DT) and a strongly diffracting η precipitate. Specimen deformed at 950 °C to a strain of 1.2 with 0.01 s^{-1}.

yield drop. There is limited evidence from the intermediate strain rate that η suppresses the RYD perhaps because it impedes the progress of the twinning and is associated with a smaller grain size.

B. *DRX and MDRX of the Two-Phase Microstructure*

Dynamic recrystallization increases with the presence of η. However, this cannot necessarily be solely attributed to the precipitates as the initial grain size of the two-phase microstructure is slightly smaller. Grain boundaries are the preferred nucleation site for recrystallizing grains; hence, DRX will be faster in finer microstructures.[9] MDRX was also found to be greater in the η samples. Figure 12 shows the recrystallized fraction with time. This trend can be described by the exponential function of the JMAK-equation[9]:

$$X_{MDRX} = 1 - exp\left(\left(\frac{t}{t_{0.5}}\right)^{n}\right) \quad [3]$$

with $t_{0.5}$ being the time for 50 pct of the microstructure recrystallized and n the Avrami exponent.[33] The Avrami exponent itself changes by η being present and its effect on the kinetics of MDRX. It is very striking from the gradients, that recrystallization in η-containing specimens is consistently slower in comparison to the single-phase microstructure. Two main microstructural reasons can explain the change the gradient. Firstly, η serves as a grain boundary pinning element. A remarkable difference in the grain size distribution could be observed between the η-containing and the η-free samples (Figure 6). The microstructure with the precipitates retained smaller grains even after the 120 seconds dwell time. The η-free samples developed a larger scatter during the hold. This observation goes in-line with the evolution of recrystallized area. The precipitates pin the grain boundaries hindering the growth of some grains during MDRX. Secondly, η locally alters the grain nucleation. Packs of η were found to inhibit recrystallization between the laths. Figure 13 shows the IPF maps of all orientations obtained from transmission Kikuchi diffraction (TKD) of a TEM foil from a sample

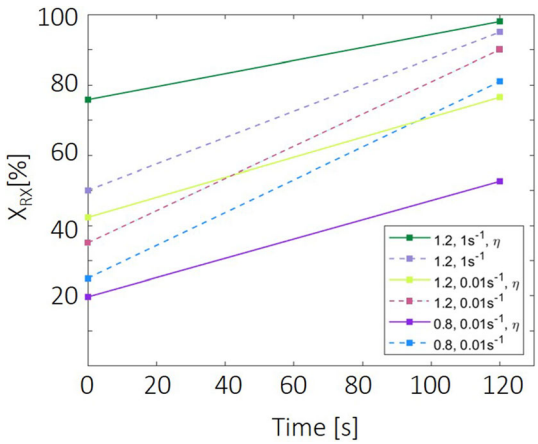

Fig. 12—Evolution of MDRX for η and η-free specimens at 975 °C for 0 and 120 seconds dwell time.

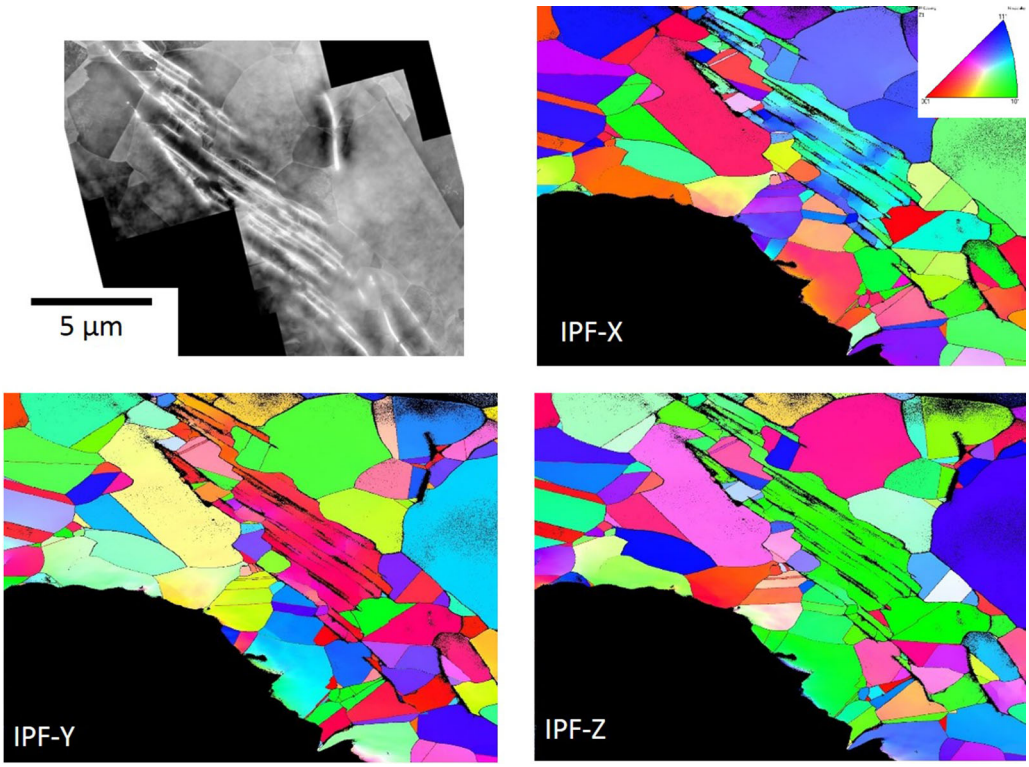

Fig. 13—Alignment of η particles with strain at 950 °C and 1 s^{-1} strain rate. In the STEM-image η are the bright precipitates while they are the unindexed pixels in the EBSD images.

which was kept in the furnace for 120 seconds after the compression. The η particles are the white lines in the STEM-HAADF image and the unindexed areas in the IPF maps appearing in dark lines. Surrounding the η pack are recrystallized grains (black circles) while within the laths the original grain orientation is still visible (white circle). In addition, there are no signs of formation of substructures between the laths which would be a precursor for recrystallization. Where recrystallization has taken place between the laths, it can be traced back to a grain penetrating through a gap in the η laths. Hence, the slower MDRX may be due to η protecting parts of the microstructure from recrystallization.

In Ni-base superalloys heteroepitaxial recrystallization was found as an additional recrystallization mechanism during high-temperature testing.[34] In comparison with PSN, a high dislocation density at the precipitates as recrystallization driving force is not necessary.[35] It was claimed to form around primary γ' based on inverse precipitation from γ' to γ. An analytical study proposed that the key feature for heteroepitaxial recrystallization to occur is the ability to form a coherent particle–matrix interface.[35] In contrast to δ in IN718, η in 718Plus can form a coherent interface $[0001]_\eta || [111]_\gamma$. Figure 14 shows a STEM-BF image of a sample compressed at 975 °C with 1 s^{-1} to 1.2. The dark η precipitates are within a larger recrystallized grain. However, some particles have a dark gray area around them with a grain boundary between the surrounding large grain. Heteroepitaxially recrystallized grains are supposed to be unstable and are consumed by growing grains.[36] However, early studies on a powder-metallurgically processed Ni-base superalloy show evidence of heteroepitaxial recrystallization in compressed samples being stable even at post-deformation soak times of 1 hour.[37] The presented image was taken from a sample which was exposed to MDRX; hence, it could be the evidence of a heteroepitaxially recrystallized grain. However, further studies are required to investigate the potential of heteroepitaxial recrystallization of η in 718Plus.

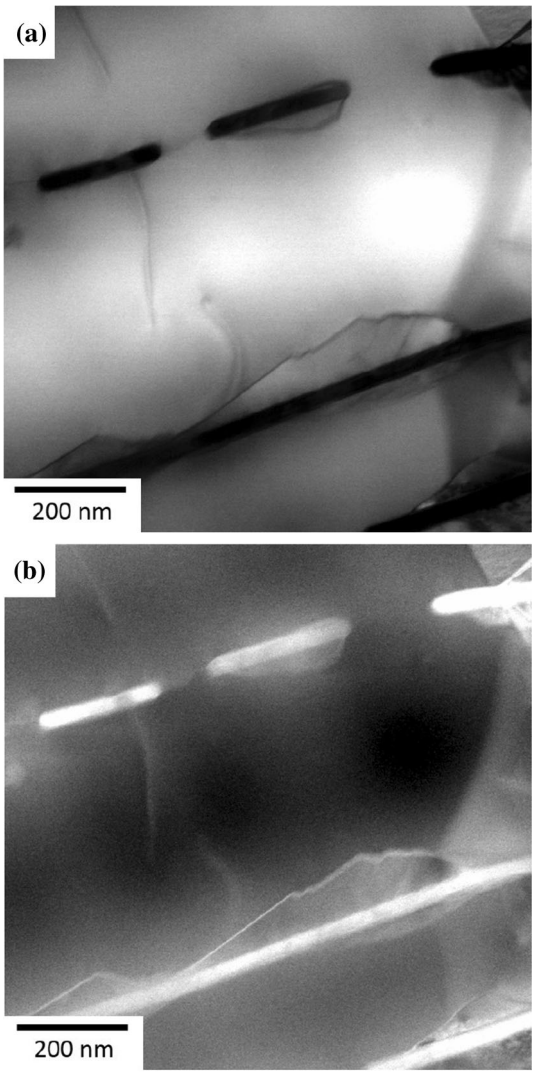

Fig. 14—STEM images of η and surrounding recrystallization of a sample tested at 975 °C,$\dot{\epsilon}$ 1 s^{-1} and ϵ 1.2. (*a*) Bright Field (BF) and (*b*) High Angle Annular Dark Field (HAADF) image.

The areas featuring small grains were located in the vicinity of the particles, giving the microstructure a heterogeneous nature. A heterogeneous microstructure can cause problems with stress concentrations in mechanical testing. Previous characterization of a forged component found a large variation in η area fraction from 2 area pct in the center to 9 area pct at the rim.[3] In terms of MDRX this scatter in the area fraction of η could lead to a wide scatter in grain sizes throughout the component.

C. *Deformation Mechanisms of* η

The η-phase showed remarkable plasticity and was found to deform either by breaking up and realigning to the flow or by severe bending of the plate-like precipitate. The two deformation mechanisms were distributed homogeneously throughout the cross-section of the sample. The η.phase deforms, but where shear on the basal plane of η is favored, lengthening of the η plates in response to the matrix deformation is difficult. So if the surrounding matrix is stretching the η breaks up. The precipitates seem able to bend and fold where the flow in γ requires this and no evidence of cracks or voids were observed.

It was shown that the precipitates gradually align themselves with strain. A strong alignment could be achieved by the breakage of the particles and subsequent spheroidization. Breakage and spheroidization of the second-phase δ in IN718 has been observed.[17] Spheroidization has been described in several alloys including titanium alloys, as a deformation mechanism of the hcp α-phase in the bcc β-matrix and in pearlitic steels during annealing.[38, 39]. The formation of a subboundary within the precipitate promotes diffusion of matrix elements to and into the particle. The matrix grows along the subboundary and into the precipitate. The particle is indented and chamfered, eventually

separating. The development of subgrains within an α-particle has been observed after deformation in Ti-6Al-2Sn-4Zr-6Mo.[40] In addition to the surface tension caused by subboundaries, dislocations moving to the particle-matrix interface can serve as stress concentrators leading to a breakage of the precipitate.[17] The smaller, round particles can then more easily align to the material flow. Figure 15(a) shows a STEM-image of a small η-precipitate ahead of a longer one (both black as they are strongly diffracting). The small η could

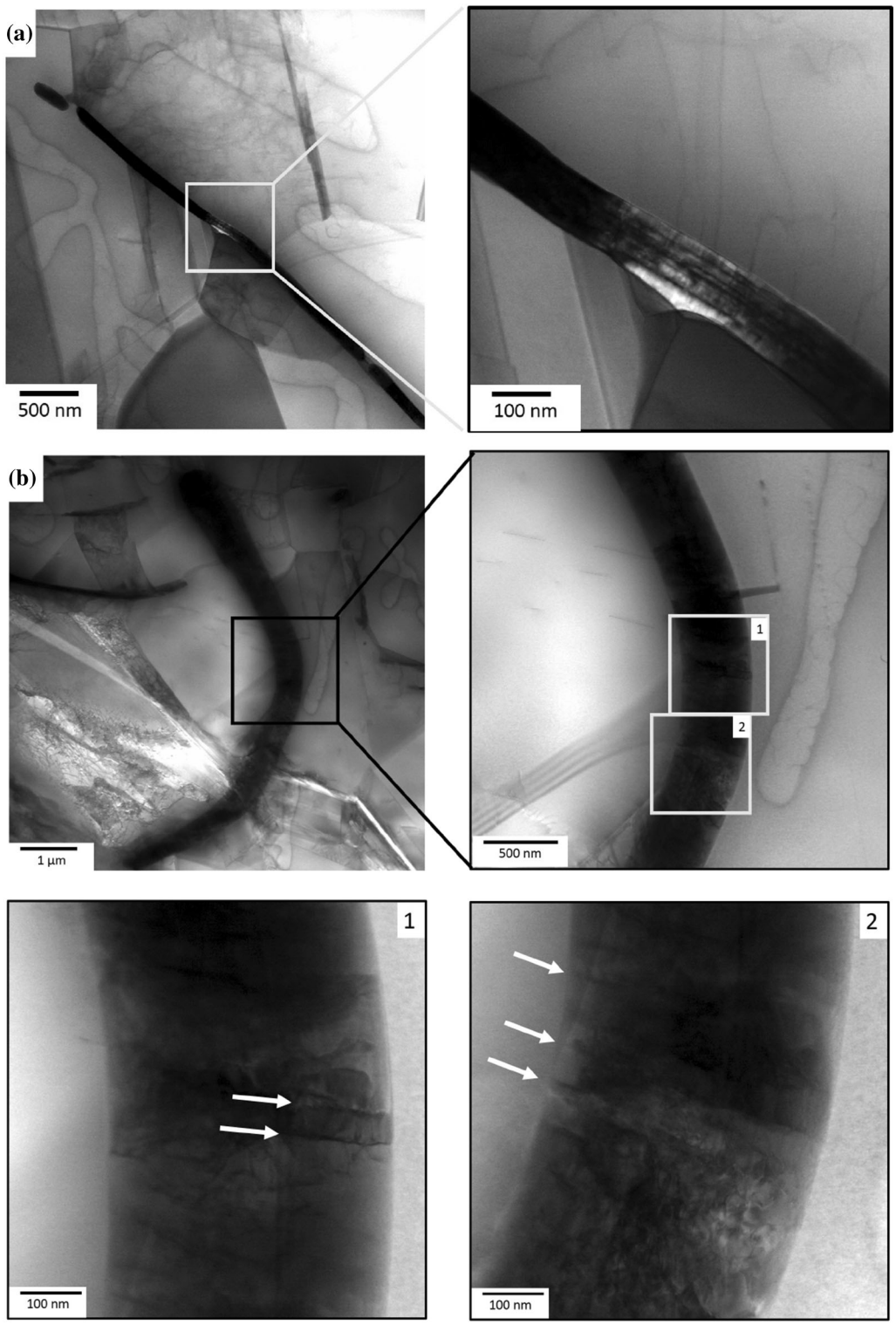

Fig. 15—STEM images of η (*a*) dissolving and breaking, (*b*) severely bent.

be the result of a spheroidization event. The microstructure of η shows darker, linear features, parallel to the closer packed planes. These features could be related to dislocation shear on the basal plane of the hexagonal η phase. The basal plane is the habit plane of the lamellae being coherent with the {111} planes of the γ matrix. If the stress state requires the precipitate to stretch (i.e., basal slip) it forces η to break and realign to the flow.

A study on δ in IN718 reports a higher degree in spheroidization in the center of the deformed samples.[17] Precipitates further away from the center were found to be in the process of breaking up with a lower occurrence of small and rounded δ. In the present study a site-specific deformation process, i.e., spheroidization in the center of the specimen and breakage at the mid-section, could not be detected.

Besides the fragmentation of η, the precipitates were also found to be able to bend by almost 180 deg without any sign of cracking. The dislocation arrangement inside severely kinked η is presented in Figure 15(b). In addition to a high dislocation density, this specific highly curved particle shows darker arrays of dislocations across the lamellae at the top end marked with white arrows. Transverse arrangement of dislocations appear to facilitate the severe curvature of the η phase. The transverse contrast observed could be due to dislocation slip on the prismatic plane. The c/a ratio of η is 1.6328[1] which is just below the transition value of 1.6333 above which basal slip is favored.[41] Bending and kinking of hexagonal precipitates is a common phenomenon for α-lamellae in titanium alloys.[42,43] The orientation of the precipitates relative to the compression axis determines the Schmid factor and hence the favored slip plane. While pyramidal slip is preferred for a deviation of the c-axis from the loading axis until 40 deg, basal slip takes over in the range between 45 to 70 deg. The prismatic slip system is activated for higher angles between c-axis and compression axis.[44]

V. CONCLUSION

The influence of the secondary η phase in the Ni-base superalloy 718Plus during hot deformation was analyzed in the present study. Particular attention was paid to the dynamic recrystallization behavior and the deformation mechanisms of η.

The stress–strain curves of the two-phase microstructure showed stronger flow softening which was found to be caused by the alignment and breakage of η. Yield point drops were observed with a clear increasing trend toward lower strain rates but an inconclusive effect of the presence of η. This phenomenon was associated with evidence of the rapid formation of deformation twinning at low strains.

Dynamic and meta-dynamic recrystallization was stronger in the η containing microstructure which was due to the difference in initial grain size. However, close lamellae of η were found to inhibit recrystallization, slowing MDRX.

The η precipitates were found to deform by either breakage and realignment with the material flow or by severe bending accommodated by ongoing recrystallization. This behavior was interpreted by hexagonal nature of η and the change in slip systems based on the Schmid Factor.

ACKNOWLEDGMENTS

The authors would like to acknowledge the support of Rolls-Royce Deutschland and Otto Fuchs KG for providing the material and also Rolls-Royce plc. and the EPSRC (Engineering and Physical Science Research Council) Strategic Partnership under EP/H022309/1 and EP/H500375/1.

REFERENCES

1. E.J. Pickering, H. Mathur, A. Bhowmik, O.M. Messe, J.S. Barnard, M.C. Hardy, R. Krakow, K. Loehnert, H.J. Stone, and C.M.F. Rae: *Acta Mater.*, 2012, vol. 60, pp. 2757–69.
2. O. Messe, J. Barnard, E. Pickering, P. Midgley, and C. Rae: *Philos. Magn.*, 2014, vol. 94, pp. 1132–52.
3. A. Casanova, N. Martin-Piris, M. Hardy, and C.M.F. Rae: *Eurosuperalloys*, 2014, vol. 1, pp. 2261–71.
4. R. L. Kennedy, Superalloys 718 and Derivatives (2005).
5. H. Zhang, C. Li, Q. Guo, Z. Ma, Y. Huang, H. Li, and Y. Liu: *Mater. Charact.*, 2017, vol. 133, pp. 138–45.
6. Y. Ning, M. Fu, and X. Chen: *Mater. Sci. Eng. A*, 2012, vol. 540, pp. 164–73.
7. Y. Wang, W. Shao, L. Zhen, and B. Zhang: *Mater. Sci. Eng., A*, 2011, vol. 528, pp. 3218–27.
8. H. Lalvani, M. Rist, and J.W. Brooks: *Prog. Adv. Mater. Res.*, 2010, vol. 91, pp. 313–18.
9. F.J. Humphreys and M. Hatherley: *Recrystallization and Related Annealing Phenomena*, 2nd ed., Elsevier, Oxford, 1996.
10. H. Lalvani and J.W. Brooks: *Metallogr. Microstruct. Anal.*, 2016, vol. 5, pp. 392–401.
11. Y. Wang, L. Zhen, W. Shao, L. Yang, and X. Zhang: *J. Alloys Compd.*, 2009, vol. 474, pp. 341–46.
12. K. Huang, K. Marthinsen, Q. Zhao, and R.E. Loge: *Prog. Mater. Sci.*, 2018, vol. 92, pp. 284–59.
13. H. Yuan and W. Liu: *Mater. Sci. Eng. A*, 2005, vol. 408, pp. 281–89.
14. P.M. Mignanelli, N.G. Jones, K.M. Perkins, M.C. Hardy, and H.J. Stone: *Mater. Sci. Eng. A*, 2015, vol. 621, pp. 265–71.

15. H. Zhang, S. Zhang, M. Cheng, and Z. Zhao: *Procedia Eng*., 2017, vol. 207, pp. 1099–104.
16. P. Paramp-Kanetas, U. Özturk, J. Calvo, J.M. Cabrera, and M. Guerrero-Mata: *J. Mater. Process. Technol*., 2018, vol. 255, pp. 204–11.
17. H. Zhang, S. Zhang, M. Cheng, and Z. Li: *Mater. Charact*., 2010, vol. 61, pp. 49–53.
18. M. Detrois, R.C. Helmink, and S. Tin: *Mater. Sci. Eng. A*, 2013, vol. 586, pp. 236–44.
19. R.L. Kennedy, W. Cao, T.D. Bayha, and R. Jeniski: *Niobium Proc. Int. Symp*., 2004, vol. 1, pp. 11–21.
20. A. Casanova, M. Hardy, and CMF. Rae: *Superalloy 718 Deriv*, 2014, vol. 1, pp. 573–86.
21. CT. Rueden, J. Schindelin, M.C. Hiner, B.E. DeZonia, E.E. Walter, E.T. Arena, and K.W. Eliceiri: *BMC Bioinf*., 2017, vol. 18, pp. 529–55.
22. D.G. Brandon: *Acta Metall*., 1966, vol. 14, pp. 1479–84.
23. C. Kienl, A. Casanova, O.M. Messe, C. Argyrakis, and C.M.F. Rae: *Superalloy 718 and Deriv*, 2018, vol. 1, pp. 405–20.
24. Y. Cao, H. Di, J. Zhang, J. Zhang, T. Ma, and R. Misra: *Mater. Sci. Eng. A*, 2013, vol. 585, pp. 71–85.
25. W.F. Smith and J. Hashemi: *Foundation of Material Science and Engineering*, McGraw-Hill, New York, 2006.
26. A. Momeni, S.M. Abbasi, M. Morakabati, and H. Badri: *Metall. Trans*., 2017, vol. 48, pp. 1216–29.
27. A.A. Guimaraes and J.J. Jonas: *Metall. Trans*., 1981, vol. 12, pp. 1655–66.
28. S. Medeiros, Y. Prasad, W. Frazier, and R. Srinivasan: *Mater. Sci. Eng. A*, 2000, vol. 293, pp. 198–207.
29. H. Monajati, M. Jahazi, S. Yue, and A.K. Taheri: *Metall. Trans*., 2005, vol. 36A, pp. 895–905.
30. A.H. Cottrell and B.A. Bilby: *Phys. Rev*., 2013, vol. 548, pp. 49–62.
31. T. Lebedkina, M. Lebyodkin, J.P. Chateau, A. Jacques, and S. Allain: *Mater. Sci. Eng. A*, 2009, vol. 519, pp. 147–54.
32. C. Kienl, F.D. Leon-Cazares, and C.M.F. Rae, Acta Mater. (2020).
33. G. Shen, S.L. Semiatin, and R. Shivpuri: *Metall. Trans*., 1995, vol. 26, pp. 1795–803.
34. M.A. Charpagne, T. Billot, JM. Franchet, and N. Bozzolo: *J. Alloys Compd*., 2016, vol. 688, pp. 685–94.
35. V.M. Miller, E.J. Payton, and A.L. Pilchak: *Scr. Metall*., 2017, vol. 136, pp. 128–31.
36. M. Charpagne, T. Billot, J. Franchet, and N. Bozzolo: *Superalloys*, 2016, vol. 1, pp. 417–26.
37. S.L. Semiatin, K.E. McClary, A.D. Rollett, C.G. Roberts, E.J. Payton, F. Zhang, and T.P. Gabb: *Metall. Trans*., 2013, vol. 44A, pp. 2778–98.
38. G. Sharma, R. Ramanujan, and G. Tiwari: *Acta Mater*., 2000, vol. 48, pp. 875–89.
39. Y.L. Tian and R.W. Kraft: *Metall. Trans*., 1987, vol. 18, pp. 1403–14.
40. M. Jackson, R. Dashwood, L. Christodoulou, and H. Flower: *J. Jpn. Inst. Light Met*., 2002, vol. 2, pp. 185–95.
41. D. Hull and D.J. Bacon: *Introduction to Dislocations*, 5th ed., Elsevier Ltd., Amsterdam, 2011, pp. 109–10.
42. S. Mironov, M. Murzinova, S. Zherebstov, G. Salishchev, and S. Semiatin: *Acta Mater*., 2009, vol. 57, pp. 1359–54.
43. R.M. Imayev, V.M. Imayev, M. Oehring, and F. Appel: *Metall. Trans*., 2005, vol. 36, pp. 859–67.
44. S. Roy and S. Suwas: *J. Alloys Compd*., 2013, vol. 548, pp. 110–25.